The Performance and Durability of High-temperature Proton Exchange Membrane Fuel Cells Enhanced by Single-layer Graphene

Jianuo Chen [a], Josh J. Bailey [b,d], Liam Britnell [c], Maria Perez-Page [a], Madhumita Sahoo [a], Zhe Zhang [a], Andrew Strudwick [c], Jennifer Hack [b], Zunmin Guo [a], Zhaoqi Ji [e], Philip Martin [a], Dan J.L. Brett [b], Paul R. Shearing [b], Stuart M. Holmes [a,*]

[a] Department of Chemical Engineering and Analytical Science, The University of Manchester, M13 9PL, United Kingdom

[b] Electrochemical Innovation Laboratory, Department of Chemical Engineering, University College London, WC1E 7JE, United Kingdom

[c] Graphene Engineering Innovation Centre, The University of Manchester, M3 3BB, United Kingdom

[d] School of Chemistry and Chemical Engineering, Queen's University Belfast, United Kingdom, BT7 1NN, United Kingdom

[e] School of Automotive Engineering, Harbin Institute of Technology, 264209, China

Corresponding author: Stuart M. Holmes, stuart.holmes@manchester.ac.uk

Abstract

Single-layer graphene (SLG) obtained by chemical vapor deposition is applied between membrane and electrodes by a wet chemical transfer method to study its effect on the performance and durability of polybenzimidazole membranes in high-temperature proton exchange membrane fuel cells (HT-PEMFCs). After accelerated stress testing (AST), the membrane electrode assembly (MEA) loaded with SLG at different positions exhibits higher peak power density, lower electrode resistances, and larger electrochemical active surface area than pure polybenzimidazole membranes with high phosphoric acid doping level. The peak power density of the MEAs with both cathode and anode loaded with SLG is 480 mW cm^{-2} after AST, while those based on pure membranes is 249 mW cm^{-2}. Lab-based X-ray micro-computed tomography combined with Raman spectroscopic mapping was applied for the first time to study the effect of SLG on controlling phosphoric acid leaching. In addition, samples containing SLG on an ultra-thin membrane (7.5 µm) were also tested to explore its influence on hydrogen crossover. After 100 hours of galvanostatic discharging, the hydrogen crossover of samples loaded with single-layer graphene on the anode does not exceed 1.75×10^{-4} mol s^{-1}, which is much lower than that of MEAs made using pure ultra-thin membranes (8.16×10^{-4} mol s^{-1}).

Keywords: Single-layer graphene; high-temperature fuel cells; chemical vapor deposition; X-ray micro-computed tomography; phosphoric acid leaching

1. INTRODUCTION

Graphene is a two-dimensional carbon nanomaterial with a hexagonal lattice structure [1]. Single-layer graphene (SLG) can block the penetration of almost all molecules and atoms including hydrogen atoms under ambient conditions [2]. Unlike its atomic form, hydrogen ions can easily penetrate graphene with a low tunnelling barrier giving SLG a high proton conductivity. The barrier to proton transport through graphene could be lower than the 1.2–2.2 eV, and the resistivity of SLG to proton can be lower than 10^{-3} Ω cm^2 when the temperature reaches 250°C [3, 4]. In addition, catalytic metal nanoparticles may enhance the proton transport capability of graphene by virtue of their high affinity for protons [2]. The presence of SLG is extremely minor, even negligible, to weaken the proton conductivity of the proton exchange membrane [5-7]. Protons can form an intermediate case between the electrons and atoms of graphene to pass through by simply tunnel [3, 8]. Transmembrane proton transport is driven by electrical polarization across the graphene layer via electrolyte solutions [9]. Combined with the above properties, SLG also has good chemical stability and excellent thermal stability, making it a promising material for proton exchange membrane fuel cells (PEMFC) [10, 11].

Although the various properties of graphene have indicated its great potential value for PEMFCs, especially its high selectivity and proton conductivity, it has only successfully been applied to direct methanol fuel cell (DMFC) [5]. The conduction of protons by typical low-temperature PEFMC based on perfluorosulfonic acid (PFSA) membranes is based on the hydration of the sulfonate group at the end of its side chain to generate ionic sites [12]. The replenishment of moisture in PFSA membranes usually depends on humidification of the gas. Therefore, the application of SLG in PEMFCs based on PFSA polymers is very likely to cause the transmission of water into the membrane to be blocked and affect the proton conductivity of the membrane [13]. Additionally, it is still a challenge to produce large-area, high-quality, low-defect SLG and transfer it to a specific substrate, which limits the application of SLG in fuel cells [5].

Different from the low-temperature PEMFC, high-temperature (HT-)PEMFC based on polybenzimidazole (PBI) and phosphoric acid (PA) conducts protons by the Grotthuss mechanism, whereby the charge carriers jump across an extended hydrogen bond network established between PBI and PA [14]. Under this mechanism, the fuel cell is no longer so dependent on humidity and the operating temperature can be higher than 100 °C [15]. Therefore, the performance of PA-doped PBI membranes largely depends on the acid doping level (ADL). However, PA leaching will inevitably occur during the operation of HT-PEMFCs [16]. In addition to being mechanically squeezed, diffusion causes PA to leach out from the membrane, when the fuel cell starts and the current increases, PA has been shown to migrate from the cathode to the anode under the influence of "electrochemical pumping" [17-19]. Moreover, PA can bleed out from the membrane since PA can be dissolved in the water produced at the cathode [20]. Excessive leaching of PA can cause the blockage of the gas diffusion layer (GDL), poisoning of the catalyst and decrease of the PA content in the membrane, thereby increasing the mass transfer resistance, reducing the activity of the oxygen reduction reaction (ORR), and

reducing the proton conductivity of the membrane, respectively [21-24]. Furthermore, weak mechanical properties of the membrane caused by high ADL and the use of ultra-thin PBI membranes (below 20 µm) may cause significant hydrogen crossover and greatly reduce the performance of the PBI membrane [25-27].

Based on the proton conduction mechanism of HT-PEMFC, the performance of PBI does not depend excessively on the entry of external substances such as water. In addition, the relatively high temperature of HT-PEMFC operation is conducive to high proton conductivity of SLG [5, 10]. Combining these characteristics, SLG is expected to become a barrier between the membrane and the catalyst layer (CL) in HT-PEMFC to prevent hydrogen crossover and excessive PA leaching.

This work aims to explore the effect of the addition of SLG, on HT-PEMFC electrochemical performance, durability, and electrochemically active surface area (ECSA) under lifetime testing or accelerated stress testing (AST). Chemical vapor deposition (CVD) method which can prepare SLG with large area, good compatibility, less disorder and fewer defects was applied [28-34]. The SLG is designed as a molecular sieve to prevent hydrogen crossover and excessive PA leaching from the membrane to the electrodes.

2. EXPERIMENTAL SECTION

2.1 SLG-based MEA preparation

The preparation of membranes and electrodes, and acid doping are shown in supporting information. SLG generation was achieved by CVD onto polycrystalline copper using methane and hydrogen as precursor gases [35, 36]. The transfer of SLG to the electrode was performed by a wet chemical transfer method and a poly(methyl methacrylate) (PMMA) layer was used as the support material for the graphene [37]. The surface of SLG prepared by CVD on a copper sheet was spin-coated with a PMMA layer. A 0.1 M ammonium persulfate aqueous solution was used to etch away the copper sheet to form a SLG-PMMA film. The detached SLG-PMMA film was washed with de-ionised water and floated on the surface of the water. The transfer of SLG-PMMA to an amorphous carbon electrode was achieved by lifting out the electrode from under the floating SLG-PMMA film. After drying at room temperature, PMMA was finally removed under acetone rinsing. The transfer of SLG and the structure of MEA are shown schematically in Figure 1.
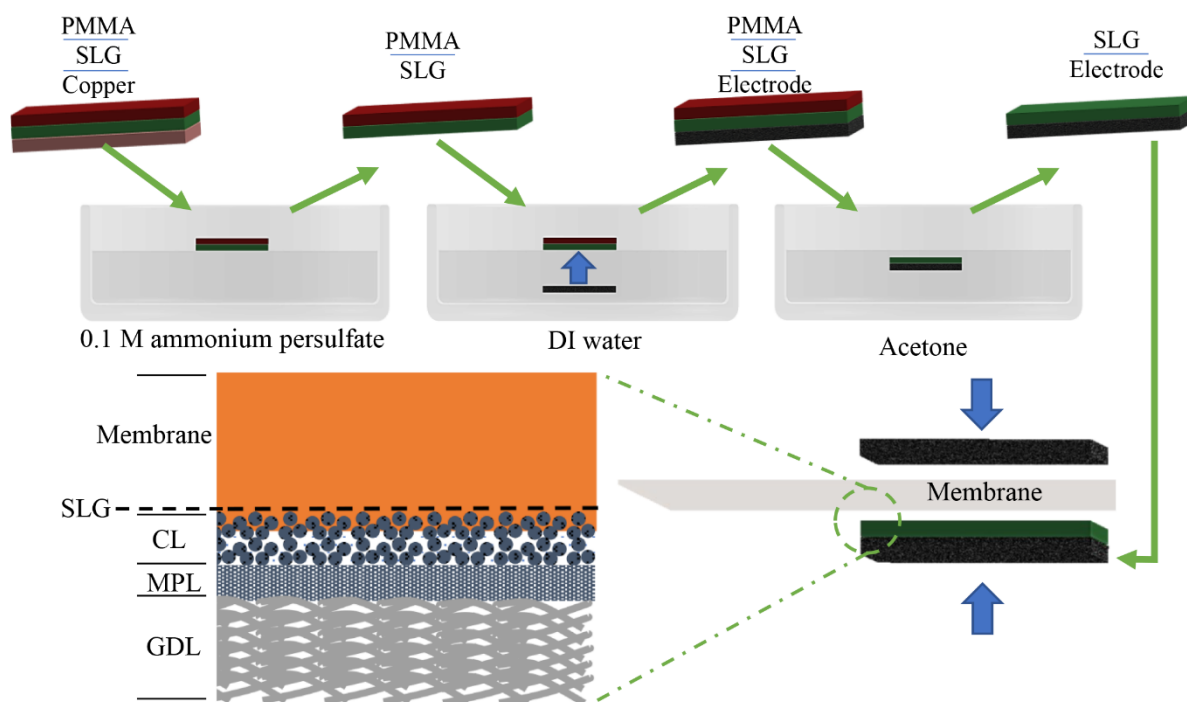
Figure 1. The transfer of SLG and the structure of membrane-electrode-assembly

2.2 Characterization of SLG and electrode coverage

Raman spectroscopy of the SLG loaded on the copper foil was performed using a Renishaw inVia™ Qontor® confocal microscope system with a 532-nm-wavelength laser. Raman acquisition of the SLG on the electrodes was carried out with the Renishaw inVia utilizing a 785-nm-wavelength laser to prevent laser damage to the catalyst surface and to reduce any fluorescence. A laser spot size of 2 μm was achieved by applying a pinhole. The coverage of SLG on electrodes was evaluated by mapping the catalyst surface and calculating the integrated peak intensity of the 2D peak.

2.3 Electrochemical characterization, performance study and MEA durability test

The prepared MEAs were assembled into an in-house fuel cell rig and operated at 150 °C with 100 mL min^{-1} dry H$_2$ and 100 mL min^{-1} dry O$_2$. A GAMRY E5000 potentiostat was used to measure linear sweep voltammetry (LSV), electrochemical impedance spectroscopy (EIS) and cyclic voltammetry (CV). Accelerated stress test (AST) is performed alternately at 0.6 A cm^{-2} (4 min) and 1A cm^{-2} (16 min), and the open circuit voltage (OCV) is operated for 10 min every 6 h. The specific parameters of electrochemical characterization are shown in supporting information.

2.4 Characterization of PA distribution and MEA component migration

A method combining lab-based X-ray CT and machine-learning segmentation has recently been established in our previous work [38]. Circular samples with a diameter of 2 mm were

milled out from MEAs by a laser micro-machining method [39] and placed on a 3D-printed multi-layer jig for X-ray CT measurement. The structure of the jig is shown in Figure S1. A Zeiss Xradia 520 Versa (Carl Zeiss) X-ray micro-CT instrument, equipped with polychromatic source and 30 to 160 kV tube voltage, was utilized to scan all samples. The specific parameters for XCT image acquisition are shown in Table S1.

Raman mapping of MEA cross-sections was carried out using a Renishaw inVia with a 785 nm laser. MEAs were manually cut by a scalpel to expose the cross-section. The resultant spectra were baseline-corrected and normalized. The free PA peak (~911 cm^{-1}) intensity was used to form the concentration maps and the distribution curves.

3. RESULTS AND DISCUSSION

3.1 SLG Coverage of Electrodes

A typical Raman spectrum of graphene prepared by CVD onto copper foil is shown in Figure 2a. The Raman spectrum only showed a G peak and a narrow 2D peak at Raman shifts of 1590 cm^{-1} and 2680 cm^{-1}, respectively. The intensity ratio of the 2D peak to the G peak (I_{2D}/I_G) was ca. 2.5, which indicates that the graphene is monolayer [40-43]. 20 × 20 μm Raman mapping with 64 points in 5 arbitrary areas across a macroscopic sample of A5 size was carried out. The I_{2D}/I_G of all of spectra exhibit same as the Raman spectrum shown in Figure 2a indicating that the graphene prepared by CVD was effectively defect-free SLG with 100% coverage of the copper foil. The graphene on the copper foil is transferred by the wet chemical transfer method. It has been shown through Raman spectroscopy that the graphene on the copper foil is a single-layer graphene. The wet chemical transfer method still maintains the graphene on the target substrate as a single layer [37]. Therefore, the thickness of graphene on the electrode surface is assumed to be about 0.335~1nm [40-43].

Although the SLG maintains good integrity on the copper sheet, SLG is prone to cracking and defect generation during transfer from the copper sheet to the target substrate [44]. The Raman spectrum of the catalyst surface is shown as the orange curve in Figure 2b. Raman spectrum on the electrode surface basically has no 2D peak. This may be attributed to the relatively weak energy of the 785 nm laser, which is not powerful enough to observe the relatively weak 2D peaks in graphite [45]. The Raman spectrum of the catalyst surface with SLG is shown in the blue curve in Figure 2b. Due to the use of electrodes with graphite-related materials as the substrate for the Raman spectroscopy, subject to the influence of the G and D peaks of the graphite materials, it is difficult for the Raman spectra of graphene on the catalyst surface to be fully consistent with the characteristics of SLG. However, the relatively strong narrow 2D peak characteristic of SLG is not completely covered by the signal from the substrate. Therefore, the 2D peak area can be used as a strong basis for whether the electrode is covered with SLG. Raman spectroscopic mapping of the 2D peak of two regions on the surface of the SLG-loaded electrode is shown in Figure 2c (Region 1) and d (Region 2). The heterogeneous distribution area of the 2D peak has obvious boundaries. The blue area is regarded as the area without graphene. The SLG coverage shown by Raman mapping in Region 1 and Region 2 is

approximately 75% and 45%, respectively, indicating the distribution of SLG in different regions may be vary to differing extents. Through multi-region Raman mapping, the average coverage of SLG on the electrode surface was measured to be ca. 55±5%.
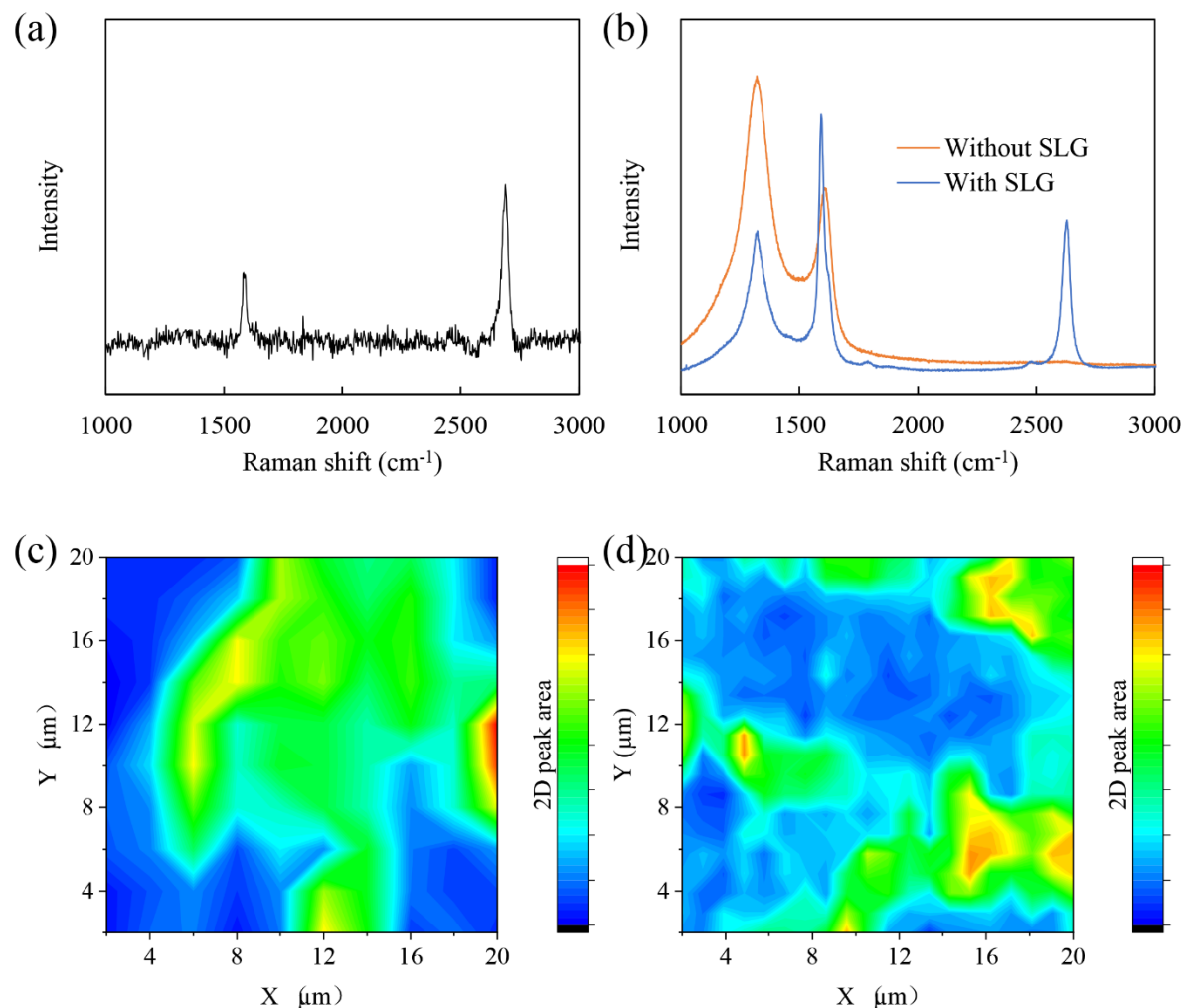

Figure 2. Raman spectrum and Raman mapping (785nm laser) of SLG on different substrates, (a) Raman spectrum of SLG on copper foil, (b) Raman spectra of electrode surface with (blue line) and without (orange line) SLG, (c) Raman mapping of electrode surface region 1, (d) Raman mapping of electrode surface region 2.

3.2 Impact of SLG on PA leaching

3.2.1 Electrochemical characterization

To explore the impact of SLG on HT-PEMFC performance and durability, SLG was loaded on anode, or cathode, or both sides. For all membranes, the ADL was approximately 11.5. MEAs without SLG, SLG on anode, SLG on cathode, and SLG on both sides are denoted PBI, AS, CS, and ACS, respectively. The naming of MEAs under different conditions is shown in Table 1. The initial measurement of MEAs is shown in Figure 3a. The peak power density of various MEAs is shown in Table 1. From the perspective of power density curves, PBI-I and CS-I have similar performance, while AS-I and ACS-I have similar but lower performance. The application of SLG did not improve the performance of HT-PEMFC in the initial measurement,

such that AS and ACS performed worse than the pristine MEAs. The difference in the performance of MEAs reflected by polarization curves in the initial measurement begins to appear at the low current density stage, which is mainly associated with activation polarization losses [46]. In the low current density stage, AS-I and ACS-I showed the most rapid voltage loss, followed by PBI-I and CS-I. The middle current density stage is dominated by ohmic losses, as the current density increases, the change in this difference is not obvious. Thus, ohmic losses is not the main cause of the difference in voltage loss [46].

Table 1. MEA nomenclature, electrochemical performance, and resistances

Name	SLG load	Condition	Peak power density (mW cm^{-2})	Ohmic resistance (mΩ cm²)	Charge transfer + mass transfer resistance (mΩ cm²)
PBI-I	No SLG	Before operation	404	201	307
AS-I	Anode side	Before operation	330	205	394
CS-I	Cathode side	Before operation	399	229	276
ACS-I	Both sides	Before operation	321	263	348
PBI-F	No SLG	After AST	249	199	414
AS-F	Anode side	After AST	367	205	355
CS-F	Cathode side	After AST	365	221	320
ACS-F	Both sides	After AST	480	205	308

The performance indicated by the final measurement of different MEAs after AST shown in Figure 3b represents a significant change compared to initial measurements. ACS-F had the highest peak power density of 480 mW cm^{-2}. AS-F and CS-F had similar peak power densities of 367 mW cm^{-2} and 365 mW cm^{-2}, while the peak power density of CS-F appeared at a lower current density. PBI-F showed the lowest peak power density, which was 249 mW cm^{-2}. From the voltage loss at different current density stages, PBI-F had the largest activation polarization losses, ohmic losses and concentration polarization losses.

The performance changes are directly reflected by the voltage changes at different current densities during the AST shown in Figure 3c. The upper, middle, and lower curves of each MEA represent the OCV, the voltage at 0.6 A cm^{-2} and the voltage at 1 A cm^{-2}, respectively. During the AST, the MEA based on a pure PBI membrane maintained a stable OCV, but the voltage at different current densities continued to drop significantly. This is generally considered to be caused by factors such as corrosion, deactivation, or migration of the internal components of the MEA, and established test methods have been shown to accelerate these aging processes [47-49]. In addition, the detrimental edge effects caused by the small electrode size and the high ADL may also accelerate the voltage drop versus other literature examples [38]. The voltage changes at different current densities are shown in Figure 4. The voltage loss of the MEA based on a pure PBI membrane at a high current density of 1 A cm^{-2} is more obvious than that at 0.6 A cm^{-2}, 43.3% and 23.6%, respectively. Different from PBI, the voltage of AS and ACS at different current densities increased versus the initial stage, rather than decreasing. This difference is reflected in the first 6-h cycle shown in the inset in Figure 3c. The
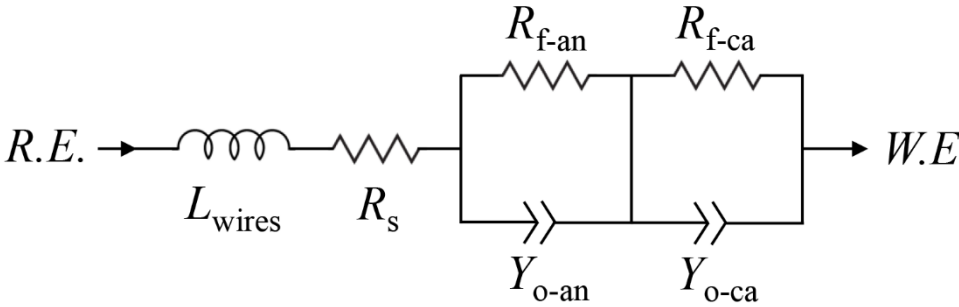
performance of PA-based HT-PEMFC continues to improve can be explained by favorable PA redistribution, the removal of impurities, or the formation of new catalytic sites that lead to the activation [50, 51]. Although the initial voltage of AS and ACS was slightly lower than that of PBI at different current densities, these values surpass that of PBI after about 7 h of AST. After 24 h, the voltage of AS remained effectively constant, while the voltage of ACS increased throughout the entire 70-h test. Although the voltage of CS continued to drop during AST, its drop is only about a quarter of that of PBI. To further test the durability of ACS, an additional 70 h of AST was run. The voltage changes at different current densities during the AST from 70 to 140 h are shown in Figure S2. In the additional AST, the voltage of the ACS at different current densities maintained a slow rise in the first 25 h. After that, the voltages remained relatively stable. At the end of the additional AST of ACS (named ACS-E), the peak power density of ACS-E reached 511 mW cm^{-2}. The polarization curve and power density curve of ACS-E are shown in Figure S3.

Nyquist curves of initial and final measurement are shown in Figure 3d and e, respectively. The equivalent circuit for fitting is shown in Table 2. The resistance between the intercept on the real Z-axis at high and low frequencies is interpreted as the sum of charge transfer resistance and mass transfer resistance of the anode and cathode, hereafter referred to as $\Delta R_{Charge+Mass}$ [52-56]. The various resistances reflected by intercepts on the real Z-axis in the Nyquist curves are summarized in Table 1. PBI-I and AS-I had very similar Ohmic resistance, which indicates that placing SLG between the anode and the PBI membrane does not cause significant hindrance to protons conduction, potentially benefitting from excellent proton conductivity of SLG and high operating temperature [2, 3]. Unlike AS-I, CS-I has lightly larger ohmic resistance and ACS-I have significantly larger ohmic resistances compared to PBI-I. That may due to SLG blocking water generated at the cathode from entering the electrolyte in a short time to hydrate and positively influence membrane conductivity [56]. Since the coverage of the SLG on the electrode is limited, long-term operation at high current density provides the possibility for the water produced at the cathode to enter the electrolyte and hydrate it. Thus, PBI-F, AS-F, CS-F and ACS-F all have closer ohmic resistance. It is worth noting that the ohmic resistance of ACS-I is significantly larger than that of CS-I, and the ohmic resistance of ACS-I before and after AST changes more than that of CS-I. This may be due to the fact that the performance of ACS in the initial stage is much lower than that of CS, resulting in that the water production of ACS-I after initial activation is much smaller than that of CS-I, so that the ohmic resistance of ACS-I is larger than that of CS-I. The difference in the impedance of each MEA is more reflected in $\Delta R_{Charge+Mass}$. The relationship between the magnitude of $\Delta R_{Charge+Mass}$ in the initial measurement of different MEAs is AS-I > ACS-I > PBI-I > CS-I. However, this relationship is completely changed in final measurement. In the final measurement, the relationship between the $\Delta R_{Charge+Mass}$ of each MEA is PBI-F > AS-F > CS-F > ACS-F. The value and change of $\Delta R_{Charge+Mass}$ may be affected by various factors such as PA migration, catalyst migration and corrosion, and the complex environment in electrodes.

The initial and final CV curves with calculated ECSA are shown in Figure 3f and g, respectively. Since the leaching of PA into the CL will poison platinum at high temperatures, and the

adsorption of phosphate anions on the catalyst surface will block catalyst active sites, *in-situ* CV measurement of HT-PEMFC is not rigorous like the low-temperature PEMFC [22, 23, 57]. The aforementioned influence of PA on the catalyst causes distortion of the CV curves such that the peak of the CV curve becomes very small [22]. The distortion of this CV peak is fully reflected in the CV curves of PBI-I and AS-I. The ECSA of PBI-I and AS-I were only 55.5 cm² mg^{-1} and 55.2 cm² mg^{-1}, respectively, and the ECSA of them dropped further after AST. However, the ECSA of the cathode of CS-I and ACS-I, is much larger than that of PBI-I and AS-I. The ECSA of the cathode of CS-I and ACS-I were 388.1 cm² mg^{-1} and 302.4 cm² mg^{-1}, respectively, which is almost 7 times that of PBI-I and AS-I. This indicates that the protection of the surface of the catalyst by SLG at the cathode is immediate. While SLG has high proton conductivity and electronic conductivity, it forms a certain isolation between PA and the surface of the catalyst that may prevent excessive phosphate anions from adsorbing onto the surface of the catalyst, thereby increasing ECSA. As for the ECSA of CS-I is higher than ACS-I, it may be due to the osmotic pressure of phosphoric acid in the membrane with SLG on both sides should be higher than when SLG is used on one side or SLG is not used on both sides. Therefore, ACS is easier to leach appropriate amount of phosphoric acid at the cathode than CS. In other words, the ACS may have more phosphoric acid covering the catalyst at the cathode. Although the ECSA of CS-F (248 cm² mg^{-1}) and ACS-F (185.8 cm² mg^{-1}) both declined compared with their respective initial values, they were still much larger than the ECSA of PBI-F (50.0 cm² mg^{-1}) and AS-F (50.8 cm² mg^{-1}). The protective capability of the catalyst by SLG is still present after AST.

Table 2. The equivalent circuit and the definition of parameters

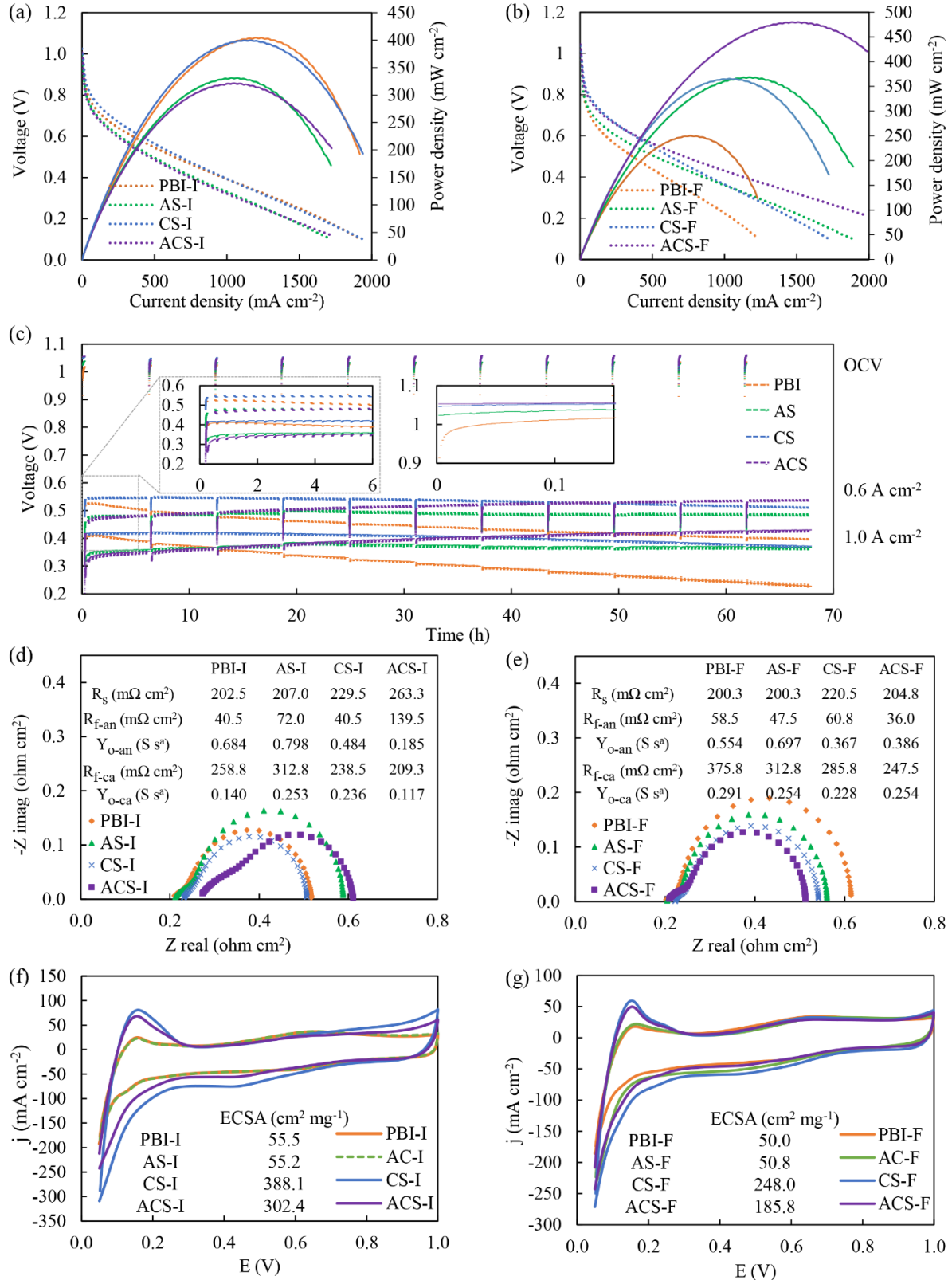| Equivalent circuit	
L_{wires} (H)	Inductance of cables
R_s (ohm)	Ohmic resistance
R_{f-an} (ohm)	Charge transfer resistance of anode
Y_{o-an} (S s^a)	Constant phase element of anode
R_{f-ca} (ohm)	Charge transfer resistance of cathode
Y_{o-ca} (S s^a)	Constant phase element of cathode
a	Dimensionless exponent

Figure 3. Electrochemical characterization: (a) initial measurement of polarization curves and power density curves (150 C°, anode: 100 mL min⁻¹ hydrogen, 1 mg cm⁻² Pt; Cathode: 100 mL min⁻¹ oxygen, 1 mg cm⁻² Pt), (b) final measurement of polarization curves and power density curves, (c) AST process, (d) initial measurement of Nyquist curves, (e) final measurement of Nyquist curves, (f) initial measurement of CV curves and (g) final measurement of CV curves (150 C°, anode: 100 mL min⁻¹ hydrogen; Cathode: 33.4 mL min⁻¹ nitrogen)
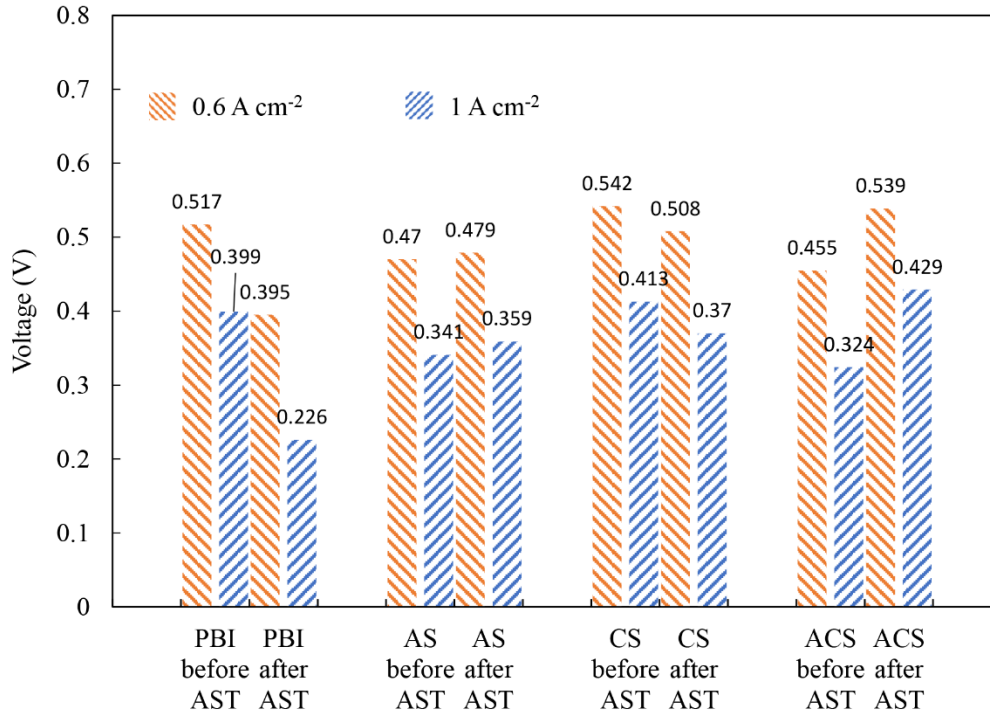
Figure 4. The voltage changes under different current densities before and after AST

3.2.2 X-ray CT

Typical 3D X-ray CT segmentations of MEA and GDL of each sample are shown in Figure 5. Since the lab-based X-ray CT in this work is unable to distinguish between (microporous layer) MPL, GDL and PA, the yellow and green phases shown in Figure 5a, c, e, g and i represent a mixture of MPL, GDL and PA of anode and cathode, respectively. GDL/MPL/(PA) composite phase may contain carbon materials, polytetrafluoroethylene (PTFE) binder, and PA. Although limited by the degree of discrimination, the distribution of the GDL/MPL/(PA) phase in the segmented XZ-orthoslice and filtered XZ-orthoslice of layer 506 in Figure 5a and c are significantly different. Compared with the pristine MEA, the yellow and green phases in the PBI-F tomogram show significant expansion, which is also accompanied by a decrease in the porosity represented by the black area. The expansion of GDL/MPL/(PA) composite phase indirectly indicates the leaching of PA, which has been demonstrated in our previous work by comparing tomograms of 'wet' electrodes soaked in PA with 'dry' electrodes [38]. This phenomenon can be more intuitively reflected in the phase fraction parameters of the GDL/MPL/(PA) composite phase shown in Table 3. The voxels of the GDL/MPL/(PA) phases in the anode and cathode of the pristine MEA account for 15.7% and 16.1% of the total 1015 × 1015 × 508 voxels. However, in PBI-F, the phase fractions of Anode GDL/MPL/(PA) phase and Cathode GDL/MPL/(PA) phase reached 22.7% and 22.6%, respectively. The CL has the greatest average X-ray attenuation coefficient due to the electron-dense Pt contained within, and thus appears brightest in orthoslice in Figure 5. Combined with the resolution used, chosen to capture a representative volume element, means the distribution of PA in the catalyst is not resolvable. However, it is not difficult to infer that the swelling of GDL/MPL/(PA) composite phase from the pristine MEA to the post-AST MEA in the electrode indicates PA leached through the CL and MPL to reach the GDL. The degree of PA migration also indicates that it

is most likely the CL is saturated with PA by the end of the AST. According to the tomographic images in Figure 4e, g and i and the phase fraction data in Table 3, it can be inferred that SLG significantly reduce the degree of PA leaching after AST. The phase fraction of the anode of AS-F is smaller than that of the cathode, being 17.4% and 21.2%, while the phase fraction of the anode of CS-F is greater than that of the cathode, being 23.7% and 19.4%, respectively. According to slice-by-slice plots of area fraction from Layer 1 to Layer 506 in the z-direction of AS-F and CS-F shown in Figure 5k and l, the above differences are mainly reflected in layers 100 to 200 and layers 300 to 400. The high phase fraction of GDL/MPL/(PA) is accompanied by the low phase fraction of pore. In the same way, the GDL/MPL/(PA) phase fraction of the anode and cathode sides of the MEA of ACS-F are relatively small, and the porosity is relatively large.

PA leaching may not only immerse the CL, but also drive the migration of the catalyst. This can be seen from the X-ray CT segmentation of the CL phase of pristine MEA and PBI-F shown in Figure 5b and d. By comparing the catalyst distribution of the SLG-loaded MEA in Figure 5f, h, j, k, l and m, the migration of the catalyst and the migration of PA are linked to a certain extent. The CL phase is more concentrated at the junction of the membrane and the electrode on the side of the electrode with SLG than on the side of the electrode without SLG.
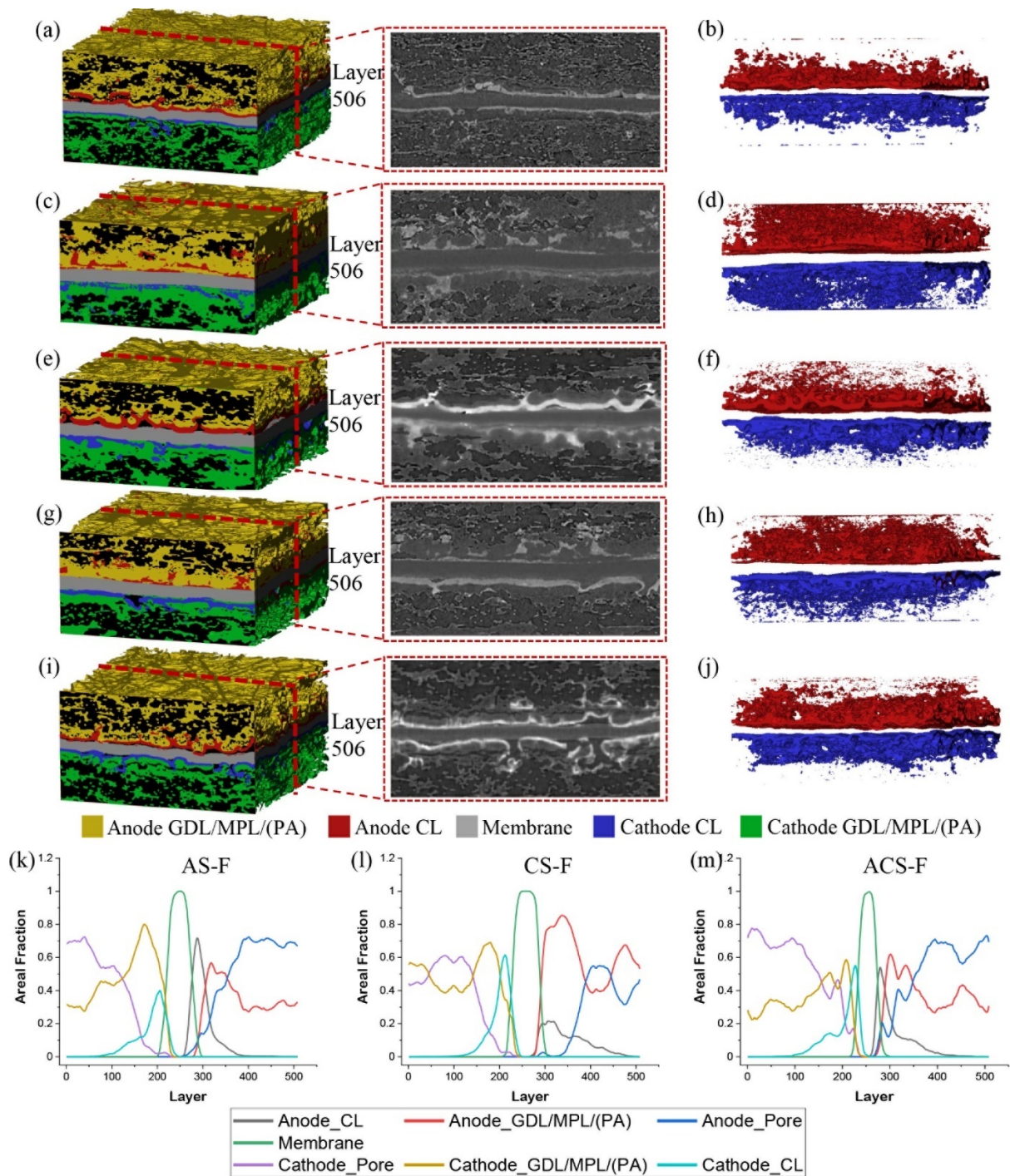
Figure 5. 3D X-ray CT segmentation of (a) pristine MEA with unsegemted orthoslice of layer 506, (b) pristine CL, (c) PBI-F MEA with unsegemted orthoslice of layer 506, (d) PBI-F CL, (e) AS-F MEA with unsegemted orthoslice of layer 506, (f) AS-F CL, (g) CS-F MEA with unsegemted orthoslice of layer 506, (h) CS-F CL, (i) ACS-F MEA with unsegemted orthoslice of layer 506 and (j) ACS-F CL. Slice-by-slice plots of area fraction from Layer 1 to Layer 506 in the Z-direction of (k) AS-F, (l) CS-F and (m) ACS-F

Table 3. Global GDL/MPL/(PA) of phase fraction of MEAs

Sample	Electrode	GDL/MPL/(PA) phase fraction	Mean
Pristine MEA	Anode	15.7%	15.9 ± 0.4%
	Cathode	16.1%	
PBI-F	Anode	22.7%	22.7% ± 0.3%
	Cathode	22.6%	
AS-F	Anode	17.4%	19.3 ± 1.3%
	Cathode	21.2%	
CS-F	Anode	23.7%	21.55 ± 3.6%
	Cathode	19.4%	
ACS-F	Anode	16.3%	16.3 ± 0.4%
	Cathode	16.2%	

3.2.3 Raman spectroscopy

X-ray CT describes the migration of components in HT-PEMFC from morphology, and Raman may prove it from a chemical point of view. Raman spectroscopy can detect the signal of free PA in the high ADL PBI membrane when the Raman shift is around 911 cm^{-1}[56, 58]. The Raman spectrum of PA-doped PBI membranes is shown in Figure 6a. The Raman spectroscopic mapping of free PA peak area of PBI-I, PBI-F, AS-F, CS-F and ACS-F in 2D form are shown in Figure 6b, c, f and h, respectively. Since Raman spectroscopic mapping is obtained by scanning the cross-sections of different samples, the thickness of each component of each sample may be different. Therefore, it is difficult to explain the migration of PA in different MEAs by comparing the size and dimension of PA distribution. However, by comparing the Raman spectroscopic mapping of PBI-I and PBI-F, free PA has a clear boundary before AST but this changes after AST. Compared with PBI-I, the free PA boundary of PBI-F shows a step-like decline from membrane to electrodes and this is more obvious in the cathode than the anode. In addition, by observing 2D Raman spectroscopic maps of AS-F, CS-F and ACS-F, the boundary of free PA on the SLG side of these MEAs is closer to the boundary between the membrane and the electrode by comparing with the 2D Raman mapping of PBI-F. The difference in the distribution of free PA in PBI-I and PBI-F as well as the influence of SLG on the migration of free PA can be shown more visually by 3D Raman spectroscopic mapping. The Raman spectroscopic mapping of PBI-I, PBI-F, AS-F, CS-F and ACS-F in 3D form are shown in Figure 6d, e, i, j and k, respectively. In contrast to the 2D mapping, the boundary of free PA of PBI-I was steeper than that of PBI-F in 3D mapping. Similarly, SLG also steepened the phosphate boundary on the additive side. The different ranges of intensity may have an impact on the degree of convergence of the PA boundary in Raman spectroscopic mappings. However, comparing the ratio of the average slope of the PA boundary between anode and cathode in 3D Raman spectroscopic mappings, hereafter referred to as $|S_{Anode/Cathode}|$, can more rigorously illustrate the influence of SLG on PA migration. $|S_{Anode/Cathode}|$ of PBI-F, AS-F and CS-F are 4.48, 7.14 and 2.11, respectively. Assuming the PA leaching situation on the side of the electrode without SLG remains unchanged, the free PA boundary on the side

with SLG function on AS-F and CS-F will be steeper than that of PBI-F. The $|S_{Anode/Cathode}|$ of ACS-F of 2.14 is similar to PBI-I of 2.91. Therefore, SLG has a buffering effect on PA leaching on its active side, which is observable by Raman spectroscopic mapping of different MEAs cross-sections. As for the obvious difference between the cathode and the anode shown in Raman spectroscopic mapping of PBI-F and AS-F, or because the uneven distribution of PA caused by the action of the "electrochemical pump" and the driving effect of the water produced by the cathode on PA. [17, 18, 20].
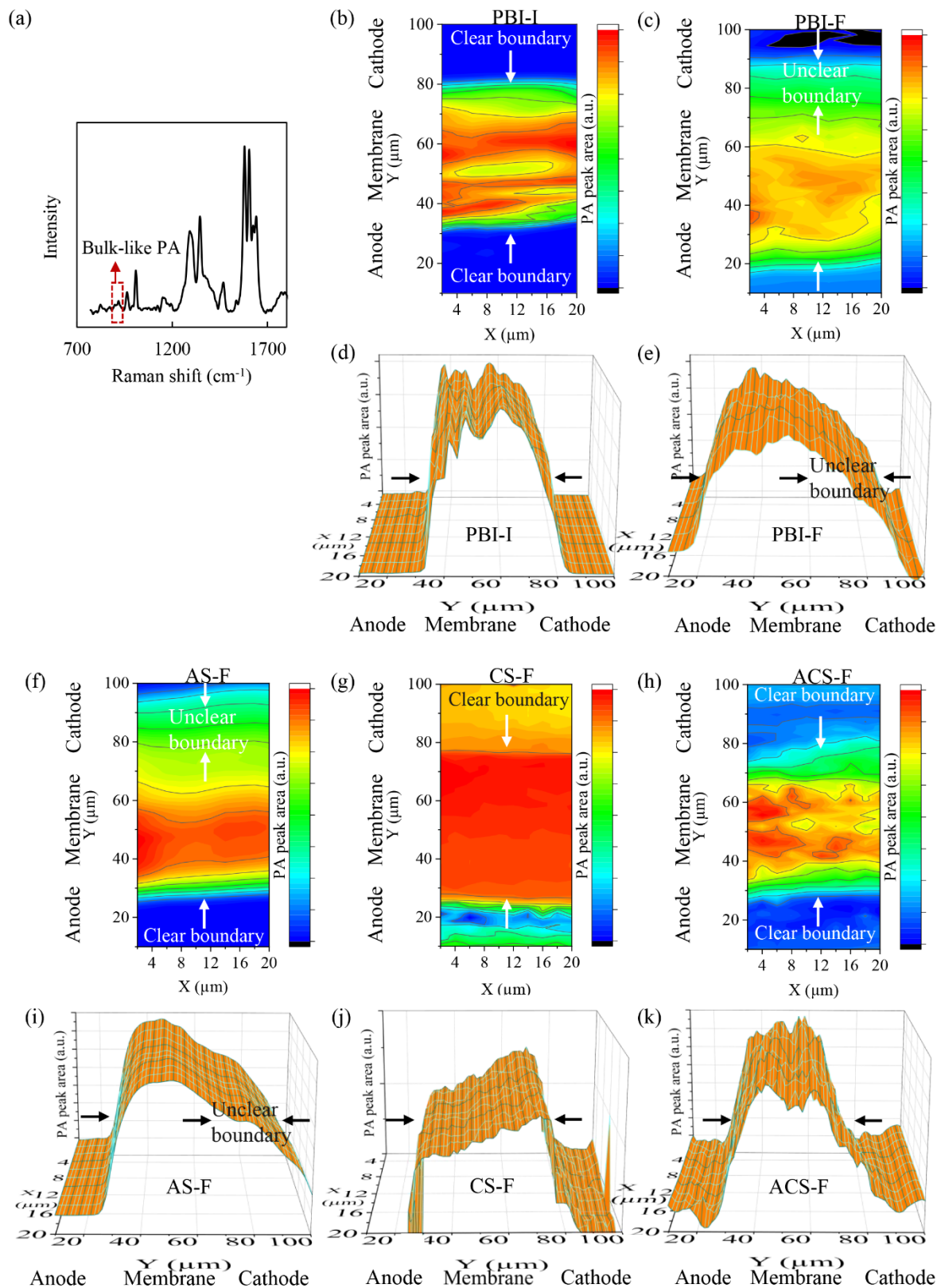
Figure 6. Raman spectrum and Raman mapping at 785 nm, (a) Raman spectrum of PA-doped PBI membrane showing free PA at 911 cm^{-1}, Raman mapping of the free PA peak at 911 cm^{-1}, (b) PBI-I in 2D, (c) PBI-F in 2D, (d) PBI-I in 3D, (e) PBI-F in 3D, (f) AS-F in 2D, (g) CS-F in 2D, (h) ACS-F in 2D, (i) AS-F in 3D, (j) CS-F in 3D, (k) ACS-F in 3D

3.2.4 Mechanism

The following mechanism for how SLG acts in a HT-PEMFC is proposed. The hydrogen oxidation reaction (HOR) and the ORR, which involve catalytic active reaction processes, mainly occur at the three-phase boundary composed of electrolyte (PA), catalyst and gas [59, 60]. Therefore, the three-phase boundary directly affects the charge transfer resistance and the activation loss in the polarization curve, and its size plays a vital role in the performance. As shown in Figure 7, the green line represents the three-phase boundary of a specific cross-section of the MEA. When PA is not leached from the PBI membrane at all, the three-phase boundary is simply the interface between the membrane and the catalyst (approximately planar under ideal circumstances). With the proper amount of PA leaching from the membrane into the CL, the three-phase boundary can be envisaged as changing from the straight green line to the wavy green line, which makes the three-phase boundary larger. This is also one of the reasons for the activation of HT-PEMFC [50, 51]. However, when PA excessively migrates into the GDL, the CL is submerged and driven to migrate, and the pores in the GDL are blocked, affecting gas transport. In these situations, the charge transfer resistance and mass transfer resistance of the MEA increase. Since the SLG prepared by CVD has good mechanical properties and good large-scale integrity, it has a good buffering effect on PA, which can be observed in X-ray CT, Raman mapping and CV. At the same time, SLG has ultra-high proton conductivity, so it does not significantly affect the transmission of protons while preventing the leaching of PA, which is reflected in EIS analysis. In summary, SLG can perform proton transfer and acts as a boundary between PA and catalyst to protect the catalyst from being soaked so that gas can reach it. Therefore, SLG can act as part of the three-phase boundary. In addition, due to the limited coverage of the SLG on electrodes, PA can still be leached out between the gaps in SLG coverage to provide a favourable distribution of PA in the vicinity of the membrane (shown in the bottom-right image in Figure 7). This is conducive to the expansion of the three-phase boundary. As mentioned above, there are different mechanisms for the leaching of phosphoric acid at the anode and cathode. During the AST process, the continuous application of higher current density and the alternating changes of the current will cause the PA to move from the cathode to the anode under the drive of the 'electrochemical pump' [17-19]. At the cathode, the production of water will also cause the leaching of phosphoric acid [20]. Therefore, the appropriate amount of PA leaching at cathode though the gap of SLG occurs at the initial stage after initial activation and is less affected by the AST process compared to the anode. It is worth noting that in the initial stage, the difference in impedance of different MEAs is mainly reflected in the $R_{f\text{-}an}$ of AS-I and ACS-I is much larger than that of CS-I and PBI-I. This results in the performance of CS-I being better than AS-I and ACS-I. With the progress of AST, the PA of AS-I and ACS-I gradually leached from the gaps of SLG to form a sawtooth-shaped phosphoric acid distribution, which increased the three-phase boundary and gradually improved the performance. This can be reflected by the impedance changes of AS and ACS before and after AST. Since CS cannot control the excessive PA leaching at anode, the performance gradually declines. In AS, the performance improvement caused by the further appropriate PA leaching at anode may be countered by the performance degradation caused by the excessive PA at cathode. Therefore, the performance of AS in the later stage of AST no longer increases, while the performance of ACS continues to increase.
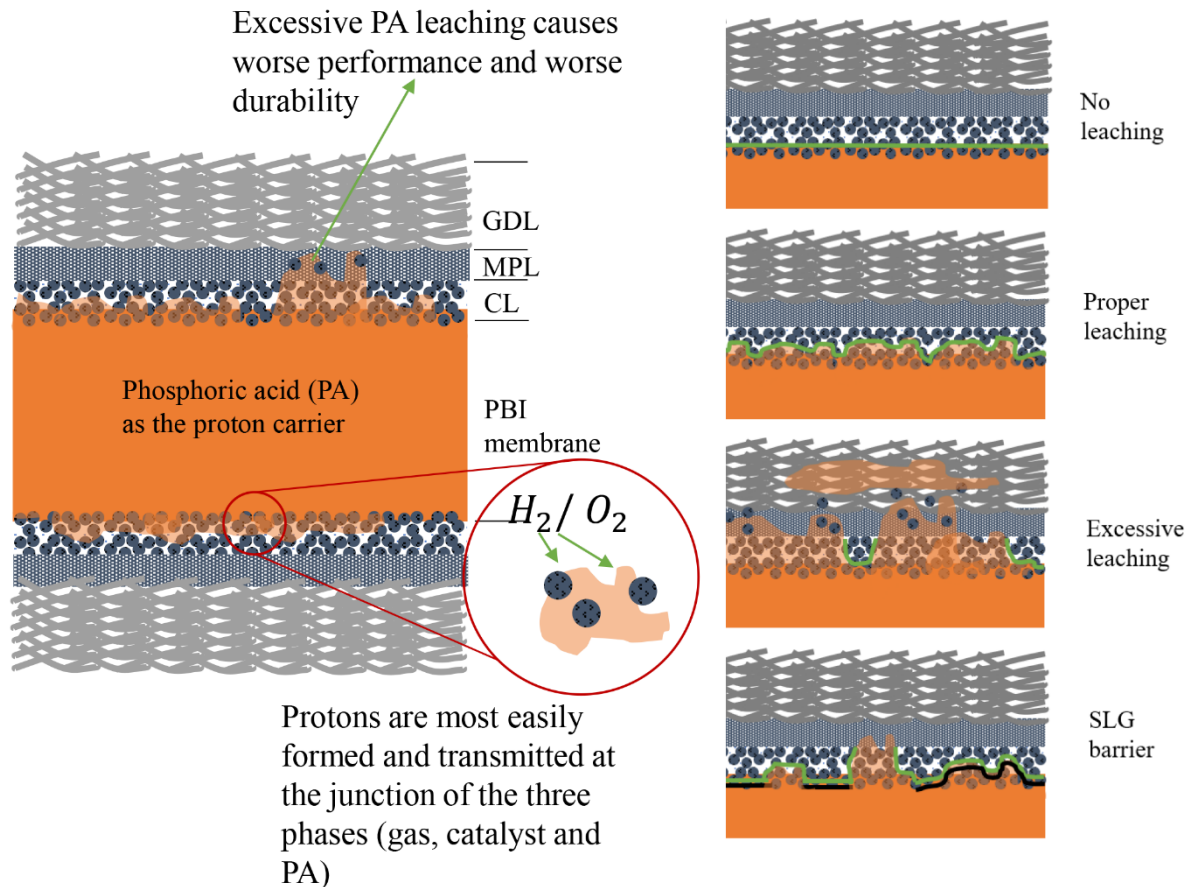
Figure 7. Proposed mechanism behind the positive effect of SLG on HT-PEMFC performance

3.3 Impact of SLG on hydrogen crossover

To explore the effect of SLG on hydrogen crossover of ultra-thin PBI (UT-PBI) membranes, a PBI membrane with a thickness of 7.7 μm was prepared, and the SLG was added between anode and membrane (UT-AS). To avoid the strong influence of AST on PA leaching, UT-PBI and UT-AS were tested under a constant current of 600 mA instead of the AST. The polarization curves and power density curves of MEAs based on ultra-thin PBI membrane under different conditions are shown in Figure 8. I and F stand for initial measurement and final measurement after 100 h testing, respectively. The ultra-thin nature of the membrane allowed for a large amount of hydrogen permeation, which gave an OCV for UT-PBI-I of only 0.57 V. Nevertheless, reducing the thickness of the membrane also reduces membrane resistance, which can be seen in the relatively low ohmic loss in the medium current density stage. This gave a relatively high maximum power density of UT-PBI-I (464 mW cm^{-2}), even higher than the maximum power density of PBI-I (404 mW cm^{-2}). The OCV for UT-AS-I of 0.80 V was significantly higher than that of UT-PBI-I, indicating that SLG had a significant blocking effect on hydrogen crossover. Although UT-PBI and UT-AS both had relatively high ADL, the ultra-thin nature made their overall PA content relatively low. Although this is helpful to avoid the side effects of excessive PA leaching, SLG may prevent the only PA in the PBI membrane from proper leaching to the electrode, leading to a dead zone between the membrane and the electrode, and the appearance of these dead zones will affect proton conduction [50, 51]. The 100-hour test of UT-PBI and UT-AS is shown in Figure 8 b. The voltage of UT-PBI continued

to drop over time. In <u>Figure 8</u> a, the polarization curve of UT-PBI-F is almost a downward shift of the polarization curve of UT-PBI-I, and the OCV of UT-PBI-F dropped from 0.57 V at the initial measurement to 0.48 V. Therefore, the continuous drop in voltage of UT-PBI during test was largely due to the gradual increase in hydrogen crossover. Unlike UT-PBI, the voltage of UT-AS continued to rise during the test. This is most likely caused by the activation of the MEA due to the reduction of the dead zone during operation [50, 51]. The OCV for UT-AS-F was effectively the same as that of UT-AS-I, which shows that there is no significant increase in hydrogen crossover during the operation of UT-AS. In addition, due to activation, the performance of UT-AS-F was significantly improved compared to UT-AS-I. The maximum power density of UT-AS-F reached 513 mW cm^{-2}, which is better than all aforementioned MEAs. The blocking effect of SLG on hydrogen crossing can be further reflected in the LSV curve shown in <u>Figure 8</u> c. The limiting current density from the LSV curves and the calculated hydrogen crossover flux are shown in <u>Table 4</u>. SLG had a certain blocking effect on the hydrogen crossover of ultra-thin PBI, and it continued to play a role throughout testing. Although SLG failed to produce an OCV at the normal level (usually considered to be 1 V), UT-AS still showed excellent performance in view of the low ohmic resistance of the ultra-thin PBI membrane.

Table 4. Hydrogen crossover flux of UT-PBI and UT-AS

MEA	$j_{H_2\ Cross}$ (mA cm^{-2})	$\dot{\eta}H_2\ Crossover$ (mol s^{-1})
UT-PBI-I	21	2.45×10^{-4}
UT-PBI-F	70	8.16×10^{-4}
UT-AS-I	14	1.63×10^{-4}
UT-AS-F	15	1.75×10^{-4}

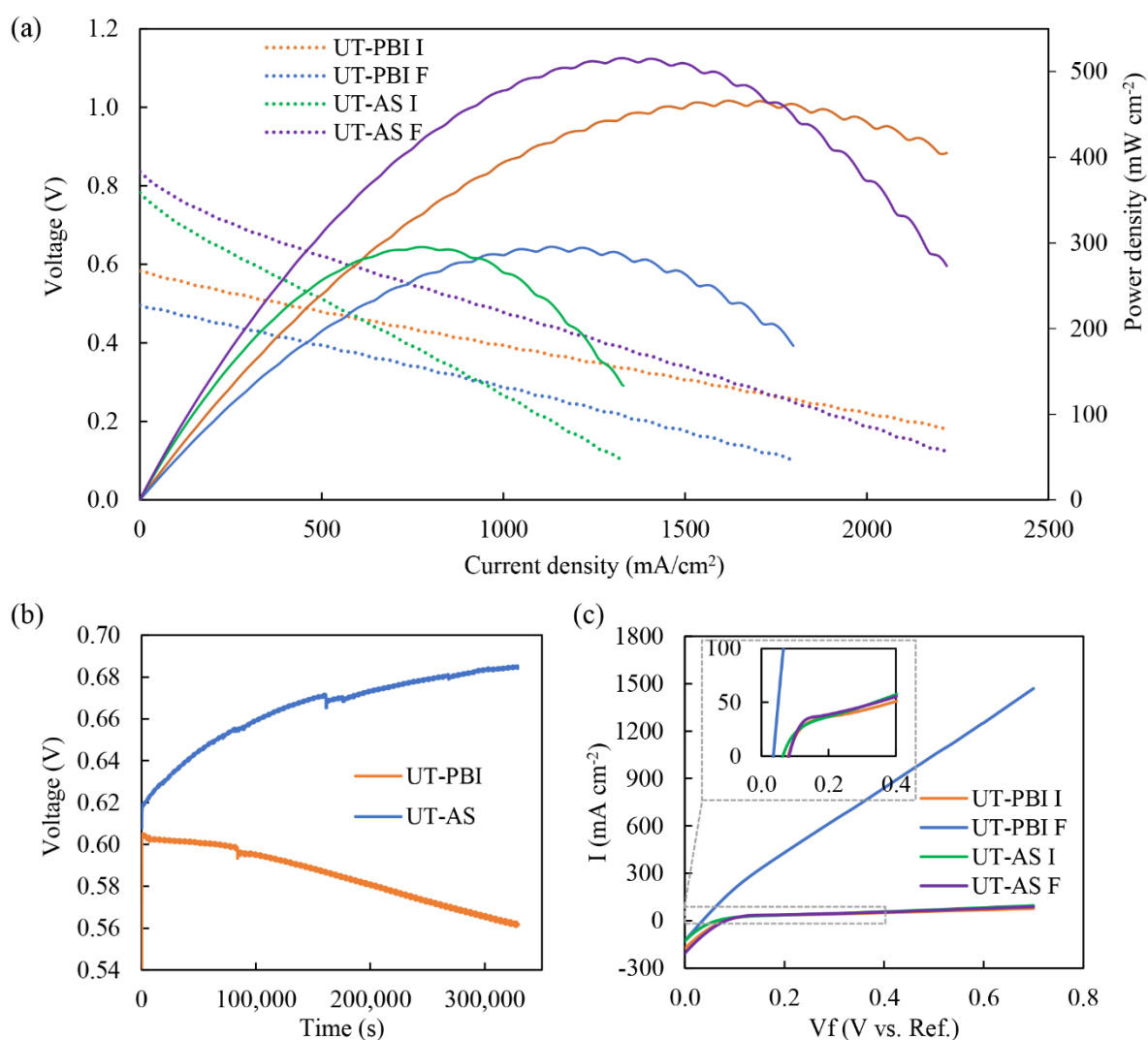*Figure 8. Electrochemical characterization of UT-PBI and UT-AS: (a) polarization curves and power density curves (150 C°, anode: 100 mL min⁻¹ hydrogen, 1 mg cm⁻² Pt; Cathode: 100 mL min⁻¹ oxygen, 1 mg cm⁻² Pt), (b) constant-current (600 mA) discharging curves, (c) LSV curves (150 C°, anode: 100 mL min⁻¹ hydrogen; Cathode: 100 mL min⁻¹ nitrogen)*

4   CONCLUSIONS

Large-size and high-quality SLG prepared by CVD was added between the membrane and anode, the cathode and both sides to study the effect of SLG on the performance and durability of PA-doped PBI membrane-based HT-PEMFC. The average coverage of the SLG on the electrode estimated by Raman spectroscopic mapping was about 55%±5%. The performance of AS-I and ACS-I, reflected by their peak power densities of 330 mW cm⁻² and 321 mW cm⁻², respectively, was significantly lower than that of PBI-I (404 mW cm⁻²). However, when the SLG is only placed on the cathode side, its effect on the initial stage performance in terms of its peak power density is not obvious (399 mW cm⁻² for CS-I). Although the SLG did not contribute to the power output in the initial stage of test, the *in-situ* ECSA of the cathode of the MEA with SLG loaded on the cathode was significantly higher than that of the PBI-I. The introduction of SLG may slow down the activation of MEAs in the initial stage caused by

advantageous PA leaching.

During AST, the performance of the MEA based on pure PBI membrane decreased significantly over time. This may be due to excessive PA leaching caused by the high ADL in the PBI affecting the three-phase boundary. The application of SLG significantly improved the durability of MEA in the AST process. The peak power density of CS-F was 365 mW cm^{-2}, which is significantly higher than that of PBI-F. For AS and ACS, the voltage at each current density during the AST process did not drop but increased, resulting in ACS-F showing the highest peak power density of 480 mW cm^{-2} across all MEAs. The resistance, ECSA, phase fraction and free PA boundary of different MEAs show that SLG can effectively control the PA leaching, maintaining a large three-phase boundary and protecting the CL.

The application of SLG can effectively limit hydrogen crossover. After 100 h of constant-current testing, hydrogen crossover of UT-AS-F and UT-PBI-F were 1.75×10^{-4} mol s^{-1} and 8.16×10^{-4} mol s^{-1}, respectively, with UT-AS-F exhibiting excellent performance with a peak power density of 513 mW cm^{-2}.

Declaration of competing interest

The authors declare that they have no known competing financial interests or personal relationships that could have appeared to influence the work reported in this paper.

References:

[1] H. Zhu, Graphene, Academic Press2018.
[2] S. Hu, M. Lozada-Hidalgo, F. Wang, A. Mishchenko, F. Schedin, R. Nair, E. Hill, D. Boukhvalov, M. Katsnelson, R. Dryfe, Proton transport through one-atom-thick crystals, Nature 516(7530) (2014) 227-230.
[3] M. Miao, M.B. Nardelli, Q. Wang, Y. Liu, First principles study of the permeability of graphene to hydrogen atoms, Physical Chemistry Chemical Physics 15(38) (2013) 16132-16137.
[4] M. Perez-page, M. Sahoo, S.M. Holmes, Single Layer 2D Crystals for Electrochemical Applications of Ion Exchange Membranes and Hydrogen Evolution Catalysts, Advanced Materials Interfaces 1801838 (2019) 1-24.
[5] S.M. Holmes, P. Balakrishnan, V.S. Kalangi, X. Zhang, M. Lozada-Hidalgo, P.M. Ajayan, R.R. Nair, 2D crystals significantly enhance the performance of a working fuel cell, Advanced Energy Materials 7(5) (2017) 1601216.
[6] X.H. Yan, R. Wu, J.B. Xu, Z. Luo, T.S. Zhao, A monolayer graphene – Nafion sandwich membrane for direct methanol fuel cells, Journal of power sources 311 (2016) 188-194.
[7] W. Jia, B. Tang, P. Wu, Novel Slightly Reduced Graphene Oxide Based Proton Exchange Membrane with Constructed Long-Range Ionic Nanochannels via Self-Assembling of Nafion, ACS applied materials & interfaces 9(27) (2017) 22620-22627.

[8] L. Britnell, R.V. Gorbachev, R. Jalil, B.D. Belle, F. Schedin, M.I. Katsnelson, L. Eaves, S.V. Morozov, A.S. Mayorov, N.M.R. Peres, A.H. Castro Neto, J. Leist, A.K. Geim, L.A. Ponomarenko, K.S. Novoselov, Electron Tunneling through Ultrathin Boron Nitride Crystalline Barriers, Nano letters 12(3) (2012) 1707-1710.

[9] S. Bukola, K. Beard, C. Korzeniewski, J.M. Harris, S.E. Creager, Single-Layer Graphene Sandwiched between Proton-Exchange Membranes for Selective Proton Transmission, ACS applied nano materials 2(2) (2019) 964-974.

[10] M. Perez-page, M. Sahoo, S.M. Holmes, Single Layer 2D Crystals for Electrochemical Applications of Ion Exchange Membranes and Hydrogen Evolution Catalysts, (2019).

[11] V. Eswaraiah, S.S.J. Aravind, S. Ramaprabhu, Top down method for synthesis of highly conducting graphene by exfoliation of graphite oxide using focused solar radiation, Journal of Materials Chemistry 21(19) (2011) 6800-6803.

[12] S.J. Peighambardoust, S. Rowshanzamir, M. Amjadi, Review of the proton exchange membranes for fuel cell applications, International journal of hydrogen energy 35(17) (2010) 9349-9384.

[13] S.A. Vilekar, R. Datta, The effect of hydrogen crossover on open-circuit voltage in polymer electrolyte membrane fuel cells, Journal of Power Sources 195(8) (2010) 2241-2247.

[14] Y.-L. Ma, J. Wainright, M. Litt, R. Savinell, Conductivity of PBI membranes for high-temperature polymer electrolyte fuel cells, Journal of the Electrochemical Society 151(1) (2003) A8.

[15] H. Su, S. Pasupathi, B. Bladergroen, V. Linkov, B.G. Pollet, Optimization of gas diffusion electrode for polybenzimidazole-based high temperature proton exchange membrane fuel cell: Evaluation of polymer binders in catalyst layer, International Journal of Hydrogen Energy 38(26) (2013) 11370-11378.

[16] S.H. Eberhardt, F. Marone, M. Stampanoni, F.N. Büchi, T.J. Schmidt, Operando X-ray Tomographic Microscopy Imaging of HT-PEFC: A Comparative Study of Phosphoric Acid Electrolyte Migration, Journal of the Electrochemical Society 163(8) (2016) F842-F847.

[17] S.H. Eberhardt, M. Toulec, F. Marone, M. Stampanoni, F. Büchi, T.J. Schmidt, Dynamic operation of HT-PEFC: in-operando imaging of phosphoric acid profiles and (re) distribution, Journal of the Electrochemical Society 162(3) (2015) F310.

[18] H.R. Kunz, Lessons Learned from Phosphoric Acid Electrolyte Fuel Cell Development Pertinent to PEMFCs, 2019, pp. 1447-1460.

[19] H. Kunz, Electrolyte migration in fuel cell modeling, J. Electrochem. Soc. Proc. 99–14 (1999) 191-207.

[20] S. Yu, L. Xiao, B.C. Benicewicz, Durability Studies of PBI-based High Temperature PEMFCs, Fuel Cells 8(3-4) (2008) 165-174.

[21] S.H. Eberhardt, F. Marone, M. Stampanoni, F.N. Büchi, T.J. Schmidt, Quantifying phosphoric acid in high-temperature polymer electrolyte fuel cell components by X-ray tomographic microscopy, Journal of synchrotron radiation 21(6) (2014) 1319-1326.

[22] S. Galbiati, A. Baricci, A. Casalegno, R. Marchesi, Degradation in phosphoric acid doped polymer fuel cells: A 6000 h parametric investigation, International journal of hydrogen energy 38(15) (2013) 6469-6480.

[23] Q. He, X. Yang, W. Chen, S. Mukerjee, B. Koel, S. Chen, Influence of phosphate anion adsorption on the kinetics of oxygen electroreduction on low index Pt(hkl) single crystals, Physical chemistry chemical physics : PCCP 12(39) (2010) 12544.

[24] Z. Guo, M. Perez–Page, J. Chen, Z. Ji, S.M. Holmes, Recent advances in phosphoric acid–based membranes for high–temperature proton exchange membrane fuel cells, Journal of Energy Chemistry (2021).

[25] H.-L. Lin, Y.-C. Chou, T.L. Yu, S.-W. Lai, Poly(benzimidazole)-epoxide crosslink membranes for high temperature proton exchange membrane fuel cells, International journal of hydrogen energy 37(1) (2012)

383-392.

[26] J.S. Yang, L.N. Cleemann, T. Steenberg, C. Terkelsen, Q.F. Li, J.O. Jensen, H.a. Hjuler, N.J. Bjerrum, R.H. He, High Molecular Weight Polybenzimidazole Membranes for High Temperature PEMFC, Fuel Cells 14(1) (2014) 7-15.

[27] G. Liu, H. Zhang, J. Hu, Y. Zhai, D. Xu, Z.-G. Shao, Studies of performance degradation of a high temperature PEMFC based on H3PO4-doped PBI, Journal of Power Sources 162(1) (2006) 547-552.

[28] P. Blake, P.D. Brimicombe, R.R. Nair, T.J. Booth, D. Jiang, F. Schedin, L.A. Ponomarenko, S.V. Morozov, H.F. Gleeson, E.W. Hill, A.K. Geim, K.S. Novoselov, Graphene-based liquid crystal device, Nano letters 8(6) (2008) 1704-1708.

[29] J. Xu, D.K. Dang, V.T. Tran, X. Liu, J.S. Chung, S.H. Hur, W.M. Choi, E.J. Kim, P.A. Kohl, Liquid-phase exfoliation of graphene in organic solvents with addition of naphthalene, Journal of Colloid And Interface Science 418 (2014) 37-42.

[30] J.N. Coleman, M. Lotya, A. O'Neill, S.D. Bergin, P.J. King, U. Khan, K. Young, A. Gaucher, S. De, R.J. Smith, I.V. Shvets, S.K. Arora, G. Stanton, H.-Y. Kim, K. Lee, G.T. Kim, G.S. Duesberg, T. Hallam, J.J. Boland, J.J. Wang, J.F. Donegan, J.C. Grunlan, G. Moriarty, A. Shmeliov, R.J. Nicholls, J.M. Perkins, E.M. Grieveson, K. Theuwissen, D.W. McComb, P.D. Nellist, V. Nicolosi, Two-dimensional nanosheets produced by liquid exfoliation of layered materials, Science (New York, N.Y.) 331(6017) (2011) 568-571.

[31] J. Liu, P. Li, Y. Chen, Z. Wang, J. He, H. Tian, F. Qi, B. Zheng, J. Zhou, W. Lin, W. Zhang, Large-area synthesis of high-quality and uniform monolayer graphene without unexpected bilayer regions, Journal of Alloys and Compounds 615 (2014) 415-418.

[32] A. Reina, X. Jia, J. Ho, D. Nezich, H. Son, V. Bulovic, M.S. Dresselhaus, J. Kong, Large area, few-layer graphene films on arbitrary substrates by chemical vapor deposition, Nano letters 9(1) (2009) 30-35.

[33] B. Sukang, K. Hyeongkeun, L. Youngbin, X. Xiangfan, P. Jae-Sung, Z. Yi, B. Jayakumar, L. Tian, K. Hye Ri, S. Young Il, K. Young-Jin, S.K. Kwang, Ö. Barbaros, A. Jong-Hyun, H. Byung Hee, I. Sumio, Roll-to-roll production of 30-inch graphene films for transparent electrodes, Nature Nanotechnology 5(8) (2010) 574.

[34] K.S. Novoselov, V.I. Fal'Ko, L. Colombo, P.R. Gellert, M.G. Schwab, K. Kim, A roadmap for graphene, Nature 490(7419) (2012) 192.

[35] C. Mattevi, H. Kim, M. Chhowalla, A review of chemical vapour deposition of graphene on copper, Journal of materials chemistry 21(10) (2011) 3324-3334.

[36] X. Li, W. Cai, J. An, S. Kim, J. Nah, D. Yang, R. Piner, A. Velamakanni, I. Jung, E. Tutuc, S.K. Banerjee, L. Colombo, R.S. Ruoff, Large-Area Synthesis of High-Quality and Uniform Graphene Films on Copper Foils, Science (American Association for the Advancement of Science) 324(5932) (2009) 1312-1314.

[37] K.S. Vasu, E. Prestat, J. Abraham, J. Dix, R.J. Kashtiban, J. Beheshtian, J. Sloan, P. Carbone, M. Neek-Amal, S.J. Haigh, A.K. Geim, R.R. Nair, Van der Waals pressure and its effect on trapped interlayer molecules, Nature communications 7(1) (2016) 12168-12168.

[38] J. Bailey, J. Chen, J. Hack, M. Perez-Page, S. Holmes, D. Brett, P. Shearing, Lab-based X-ray micro-computed tomography coupled with machine-learning segmentation to investigate phosphoric acid leaching in high-temperature polymer electrolyte fuel cells, Journal of Power Sources 509 (2021) 230347.

[39] J.J. Bailey, T.M.M. Heenan, D.P. Finegan, X. Lu, S.R. Daemi, F. Iacoviello, N.R. Backeberg, O.O. Taiwo, D.J.L. Brett, A. Atkinson, P.R. Shearing, Laser-preparation of geometrically optimised samples for X-ray nano-CT, Journal of microscopy (Oxford) 267(3) (2017) 384-396.

[40] C.F. Andrea, M.B. Denis, Raman spectroscopy as a versatile tool for studying the properties of graphene, Nature Publishing Group, 2013, p. 235.

[41] A.C. Ferrari, Raman spectroscopy of graphene and graphite: Disorder, electron–phonon coupling,

doping and nonadiabatic effects, Solid State Communications 143(1-2) (2007) 47-57.

[42] L.M. Malard, M.A. Pimenta, G. Dresselhaus, M.S. Dresselhaus, Raman spectroscopy in graphene, Physics Reports 473(5) (2009) 51-87.

[43] Z. Ni, Y. Wang, T. Yu, Z. Shen, Raman spectroscopy and imaging of graphene, Nano research 1(4) (2008) 273-291.

[44] C.e.N.e.R. Rao, A.e.K. Sood, K.e.S. Subrahmanyam, A. Govindaraj, Graphene: the new two-dimensional nanomaterial, Angewandte Chemie International Edition 48(42) (2009) 7752-7777.

[45] R. Yivlialin, L. Brambilla, G. Bussetti, M. Tommasini, A.L. Bassi, C.S. Casari, M. Passoni, F. Ciccacci, L. Duò, C. Castiglioni, Evolution of the graphite surface in phosphoric acid: an AFM and Raman study, Beilstein journal of nanotechnology 7(1) (2016) 1878-1884.

[46] F. Barbir, PEM fuel cells theory and practice, 2nd ed. ed., Amsterdam ; Boston : Elsevier/Academic Press, Amsterdam ; Boston, 2013.

[47] F.J. Pinar, M. Rastedt, N. Bruns, P. Wagner, Accelerated Stress Testing of Polybenzimidazole based HT-PEM Fuel Cells from Different Suppliers,   (2013).

[48] Y. Zhai, H. Zhang, G. Liu, J. Hu, B. Yi, Degradation Study on MEA in H[sub 3]PO[sub 4] / PBI High-Temperature PEMFC Life Test, Journal of the Electrochemical Society 154(1) (2007) B72.

[49] D. Schonvogel, M. Rastedt, P. Wagner, M. Wark, A. Dyck, Impact of Accelerated Stress Tests on High Temperature PEMFC Degradation, Fuel cells (Weinheim an der Bergstrasse, Germany) 16(4) (2016) 480-489.

[50] S. Galbiati, A. Baricci, A. Casalegno, G. Carcassola, R. Marchesi, On the activation of polybenzimidazole-based membrane electrode assemblies doped with phosphoric acid, International Journal of Hydrogen Energy 37(19) (2012) 14475-14481.

[51] M. Boaventura, A. Mendes, Activation procedures characterization of MEA based on phosphoric acid doped PBI membranes, International Journal of Hydrogen Energy 35(20) (2010) 11649-11660.

[52] P. Zoltowski, A new approach to measurement modelling in electrochemical impedance spectroscopy, Journal of electroanalytical chemistry (Lausanne, Switzerland) 375(1) (1994) 45-57.

[53] S.J. Andreasen, J.L. Jespersen, E. Schaltz, S.K. Kær, Characterisation and Modelling of a High Temperature PEM Fuel Cell Stack using Electrochemical Impedance Spectroscopy, Fuel cells (Weinheim an der Bergstrasse, Germany) 9(4) (2009) 482-482.

[54] X. Yuan, H. Wang, J. Colin Sun, J. Zhang, AC impedance technique in PEM fuel cell diagnosis—A review, International journal of hydrogen energy 32(17) (2007) 4365-4380.

[55] N. Wagner, Characterization of membrane electrode assemblies in polymer electrolyte fuel cells using a.c. impedance spectroscopy, Journal of Applied Electrochemistry 32(8) (2002) 859-863.

[56] M. Mamlouk, K. Scott, Analysis of high temperature polymer electrolyte membrane fuel cell electrodes using electrochemical impedance spectroscopy, Electrochimica acta 56(16) (2011) 5493-5512.

[57] A. Orfanidi, M.K. Daletou, L. Sygellou, S.G. Neophytides, The role of phosphoric acid in the anodic electrocatalytic layer in high temperature PEM fuel cells, Journal of applied electrochemistry 43(11) (2013) 1101-1116.

[58] F. Conti, A. Majerus, V. Di Noto, C. Korte, W. Lehnert, D. Stolten, Raman study of the polybenzimidazole-phosphoric acid interactions in membranes for fuel cells, Physical chemistry chemical physics : PCCP 14(28) (2012) 122-126.

[59] P. KURzwEIL, Brennstoffzellentechnik—Grundlagen, Komponenten, Systeme, Anwendungen. Friedr. Vieweg & Son Verlag/GWV Fachverlag GmbH, Wiesbaden   (2003).

[60] J. Zhang, PEM Fuel Cell Electrocatalysts and Catalyst Layers: Fundamentals and Applications, 1. Aufl.

ed., Springer Verlag London Limited, London, 2008.

Vitae
Jianuo Chen

Jianuo Chen is currently a Ph.D. candidate in Department of Chemical Engineering and Analytical Science at the University of Manchester, UK. He has obtained master and bachelor's degrees from the University of Manchester and Dalian University of Technology, respectively. His research field is the application of graphene–related materials in high–temperature proton exchange membrane fuel cells.

Josh J. Bailey

Dr Josh J. Bailey is currently working as a Research Fellow in the School of Mechanical and Aerospace Engineering at Queen's University Belfast (QUB), after having worked as a Post-Doctoral Research Associate and completing his PhD in the Electrochemical Innovation Laboratory at University College London. His research is related to electrochemical energy storage, including polymer electrolyte fuel cells, solid oxide fuel cells, lithium-ion and solid-state batteries, and redox flow batteries. His interests also lie in advanced characterisation techniques, such as X-ray computed tomography and focused-ion beam/scanning electron microscopy, and the application of polymer nanocomposites and biomass-derived materials to sustainable applications.

Liam Britnell
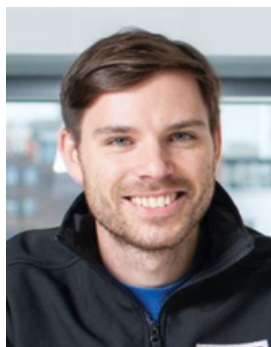
Dr Liam Britnell is an Application Manager at The University of Manchester, where he leads the printed electronics team which collaborates with industry on developing processes for scale up and cost down of printed 2D material applications in wireless communication, electrochemical sensing and smart surfaces. He has been active in the graphene and 2D materials research world for over 12 years, with roles in both research at The University of Manchester and industry for several material technology start-up companies.

Maria Perez-Page

Dr. Maria Perez-Page, Lecturer in the Department of Chemical Engineering at the University of Manchester. Her research is focused on the design and development of high selective membrane for the application on different electrochemical energy devices such as fuel cells, redox flow batteries and electrolysers. She is focusing on different polymer materials to synthesized functionalised-GO composite membranes to less prone the crossover of key species, but at the same time allowing ion conductivity. Additionally, she develops catalyst to enhance the performance of the reactions involved in fuel cells and electrolysers using 2D materials. Her ultimate aim is to develop strong and versatile understanding than can be applied for the development of ion-exchange membranes and catalyst for a wide range of electrochemical applications.

Madhumita Sahoo

Madhumita Sahoo has worked as a research associate at the Department of Chemical Engineering and Analytical Science, University of Manchester, UK. Her research was focused on 2D materials for low and high-temperature proton exchange membrane fuel cell (PEMFC) electrolytes. She received her Doctorate degree from the Department of Physics, Indian Institute of Technology Madras, India on hybrid nanostructures for low-temperature PEMFC cathode catalysts and lithium-ion battery anode materials. She has worked as a project officer for sodium-ion battery anode materials at IITM prior to joining UoM. She is currently working as fuel cell materials lead engineer at Volvo Technology AB, Sweden.

Zhe Zhang

Dr Zhe Zhang has worked as a research associate at the Department of Chemical Engineering and Analytical Science. He obtained his PhD at the University of Manchester before this role. His research focused on the in-situ measurement of proton exchange membrane in working fuel cells with spectroscopy. He is an in-situ Raman and Infrared specialist with more than five years of experience in data analysis, especially sample imaging and machine learning. He has applied those analysis methods to study the degradation of DMFC and PEMFC caused by mass transfer, such as methanol crossover and phosphoric acid leakage. He also has experience in researching living cell and biopsy samples in clinical translation and assisted cancer diagnosis.

Andrew Strudwick

Dr. Andrew James Strudwick is a Senior Applications Specialist at the University of Manchester, working in the deposition lab which carries out collaborate research projects with industrial partners with an aim to commercialise graphene and 2D materials research. Andrew has over 12 years' experience of researching graphene and 2D materials and has held research positions at both SME and large companies.

Jennifer Hack

Dr Jennifer Hack is an EPSRC Doctoral Prize Fellow, based at the Electrochemical Innovation Lab (EIL), University College London. Her work focuses on 3- and 4D characterisation of electrochemical energy devices and she uses X ray and neutron imaging techniques to probe the complex relationship between electrode morphology and electrochemical performance. During her PhD, Jennifer used such techniques to understand the operation and degradation of low temperature, polymer electrolyte fuel cells. Her current work uses similar methods to understand the morphology changes occurring in zinc-air batteries during cell cycling.

Zunmin Guo

Zunmin Guo is currently a Ph.D. candidate in Department of Chemical Engineering and Analytical

Science at the University of Manchester, UK. He received his master's degree in advanced chemical engineering from the University of Manchester in 2017. Afterwards, he worked as a Quality Assurance in STA Pharmaceutical Co. Ltd. for two years. His current research interest is mainly focused on the proton exchange membranes and new energy 2D materials.

Zhaoqi Ji

Zhaoqi Ji is currently a Lecturer in the School of Automotive Engineering at Harbin Institute of Technology, China. He graduated with a PhD in Chemical Engineering and Analytical Science from the University of Manchester, UK. He obtained his Bachelor and Master's degrees in environmental engineering from Inner Mongolia University in 2016 and Hong Kong University of Science and Technology in 2017, respectively. His research focuses on the application of novel materials and the design of membrane electrode assembly (MEA) structure in Proton Exchange Membrane Fuel Cells.

Philip Martin

Philip Martin is a Professor in the Department of Chemical Engineering and Analytical Science. He has a first degree in Chemistry from the University of Oxford and a PhD from Cambridge in physical chemistry in the group of Professor Paul Davies. Following this he held a Royal Society European Fellowship at the Universite de Paris-Sud/CNRS in Orsay in the group of Guy Guelachvili. Following this he spent three years in the group of Professor John Maier FRS at the University of Basel in Switzerland where he worked on laser spectroscopy of free radicals and molecular ions.

Dan J.L. Brett

Professor Dan Brett received his Ph.D. in Physical Chemistry from Imperial College London in 2000. After further research positions at Imperial, he joined the Department of Chemical Engineering at UCL in 2007 where his is currently Professor of Electrochemical Engineering and co- Director of the Electrochemical Innovation Lab (EIL). His main research interest is in the area of electrochemical energy conversion and storage, and he is passionate about translating early-stage innovation into marketable technology.

Paul R. Shearing

Prof Paul Shearing is the Royal Academy of Engineering Chair in Emerging Battery Technologies for Next Generation Energy Storage, based in Dept. Chemical Engineering at UCL. He is a co-director of the Electrochemical Innovation Lab and from 2012-16 he was a holder of a Royal Academy of Engineering Research Fellowship. His research interests cover a broad range of electrochemical engineering themes with a particular interest in the relationship between performance and microstructure for energy materials.

Stuart M. Holmes

Stuart M Holmes is a Professor and Head of research at the Department of Chemical Engineering and Analytical Science, University of Manchester. He is a Chemist by first degree, and he did his Ph.D. with Prof. John Dwyer, one of the founding fathers of zeolite chemistry. He was manager of the UMIST Centre for Microporous Materials prior to joining the University of Manchester. His recent research has been focused on enhancing performance of PEM fuel cells utilising novel materials and composites as membranes or catalyst supports.